The Astronomical Journal, 124:1918–1933, 2002 October

THE MX NORTHERN ABELL CLUSTER SURVEY II: THE ABELL/ACO CLUSTER REDSHIFTS AND SPATIAL ANALYSES

Christopher J. Miller,[1,2] K. Simon Krughoff,[1] David J. Batuski,[1] and John M. Hill[3]

Received 2002 February 19; accepted 2002 June 24

ABSTRACT

The MX Northern Abell Cluster Survey II is the final stage of a program designed to observe rich Abell clusters with $m_{10} \leq 17.0$. We present 1542 new galaxy redshifts within 117 $R \geq 1$ Abell cluster fields that have $16.9 \leq m_{10} \leq 17.0$, $0^{\rm h} \leq \alpha \leq 24^{\rm h}$, $-17^\circ \leq \delta \leq 90^\circ$, and $|b| \geq 30^\circ$. Of the 117 clusters observed for the MX Survey II, 105 new cluster redshifts were obtained with an average of eight cluster member galaxy redshifts. We update the m_{10}-z estimator for Abell clusters and calculate the spatial number density of Abell clusters to be $\bar{n}_c = (8.25 \pm 1.9) \times 10^{-6}\, h^3$ Mpc^{-3} within $z = 0.10$. All $R \geq 1$ Abell and ACO clusters with measured redshifts were combined to calculate the two-point spatial correlation function $\xi(r) = (r/r_o)^\gamma$ for the largest complete sample of rich clusters to date. We find $18.6 \leq r_o \leq 21.0\ h^{-1}$ Mpc and $-2.03 \leq \gamma \leq -1.95$. The slope and correlation length are very robust and remain unaffected by the exclusion of compact and dense superclusters or by accounting for line-of-sight anisotropies, which are explained by the existence of three observationally confirmed and extended superclusters.

Key words: galaxies: clusters: general — large-scale structure of universe — surveys

On-line material: machine-readable tables

1. INTRODUCTION

The complete three-dimensional mapping of the universe to 300 h^{-1} Mpc (estimated magnitude limit: $m_V \simeq 18.3$) is an immense process, requiring roughly one million galaxy redshifts (throughout this work we use a Friedmann universe with $q_0 = 0$ and $H_0 = h = 100$ km s^{-1} Mpc^{-1}). Fortunately, two wide-area galaxy surveys are currently underway: the 2dF Galaxy Redshift Survey in the southern hemisphere (see Lewis, Glazebrook, & Taylor 1998; Colless et al. 2001) and the Sloan Digital Sky Survey (SDSS) in the north (York et al. 2000). Together, the SDSS and 2dF surveys will observe spectroscopically well over one million galaxies and half a million quasars. Meanwhile, the study of large-scale structure remains crucial to understanding cosmological implications of the *COBE* results, which indicate that structure was once present on 100 h^{-1} Mpc and larger scales (Smoot et al. 1992). In addition, there have been discoveries of superclusters over 150 h^{-1} Mpc in length (e.g., Batuski et al. 1999). It is structure on these extremely large scales that can only be probed through large area and deep redshift surveys (see, e.g., Miller & Batuski 2001).

The MX Northern Abell Cluster Survey was initiated to study these large scales optically using a minimal amount of telescope time. At the start of this project, the scale of the largest features detected through individual galaxy redshifts was near the upper limit set by the depth of the surveys. For the CfA surveys (see, e.g., Geller & Huchra 1989; Postman, Huchra, & Geller 1992, hereafter PHG92) this corresponds to a depth of 12,000 km s^{-1} ($\sim$120 h^{-1} Mpc). The Las Campanas Redshift Survey contains $\simeq$26,000 galaxy redshifts out to $cz \simeq 30{,}000$ km s^{-1} ($\sim$300 h^{-1} Mpc) but only covers 700 deg^2 (Shectman et al. 1996). Because of the difficulties involved in complete galaxy mapping, such as time constraints and data storage, alternative methods for analyzing large-scale structure have been employed. Two examples of these alternate approaches are pencil-beam surveys (see e.g., Broadhurst et al. 1990) and the use of a population of sparse tracers such as from the *IRAS* point-source catalog, also known as the QDOT redshift survey and the more recent PSCz galaxy survey (Rowan-Robinson et al. 1990; Saunders et al. 2000). We have chosen to use clusters of galaxies as our sparse tracer of the true luminous mass distribution of the universe. Abell's (1958) $R \geq 1$ galaxy clusters are ideally rare for large-scale structure studies. They have an average spatial separation of $\simeq$55 h^{-1} Mpc, making them efficient samplers of the mass distribution on scales larger than 100 h^{-1} Mpc. A minimum of telescope time is required to map such large scales with clusters, since spectroscopy of only a few relatively bright galaxies is needed to obtain a reliable redshift for a cluster.

While most early cluster work was based on visually selected galaxy clusters (i.e., the Abell/ACO, Automatic Plate Measuring Facility [APM; Maddox, Efstathiou, & Sutherland 1990a; Maddox et al. 1990b], and Edinburgh-Durham Southern Galaxy [Nichol et al. 1992] cluster catalogs), there has been ample research on X-ray–selected (or confirmed) cluster samples. Examples of modern X-ray cluster samples and their use in studying large-scale structure include Romer et al. (1994), Ebeling et al. (1997), Moscardini et al. (2000), Romer et al. (2000), Collins et al. (2000), and Cruddace et al. (2002). X-ray–selected cluster catalogs can avoid visual selection or projection biases since the thermal X-ray emission from intracluster gas confined to the gravitational potential wells of galaxy clusters is typically bright and highly peaked at the gravitational center of the clusters. Unfortunately, X-ray cluster observations are expensive, requiring significant time on space telescopes. An X-ray

[1] Department of Physics and Astronomy, University of Maine, Orono, ME 04469.

[2] Department of Physics and Astronomy, Carnegie Mellon University, 5000 Forbes Avenue, Pittsburgh, PA 15213.

[3] Steward Observatory, University of Arizona, 933 North Cherry Avenue, Tucson, AZ 85721-0065.

survey of the sky with the sensitivity needed to find all clusters within $z = 0.15$ would require a fully dedicated telescope.

There are differences between X-ray–selected and optically selected clusters. Burke, Collins, & Mann (2000) found that the brightest cluster galaxies are more luminous and more uniform in high L_X clusters than in their low L_X counterparts. Donahue et al. (2001) and Donahue et al. (2002) used an optical matched-filter technique, as well as an X-ray cluster finding technique, to create optical and X-ray catalogs on the same portion of the sky. They found that (1) there is a population of rich matched-filter clusters that are underluminous in the X-ray and (2) some of their X-ray–selected clusters lack a prominent color-magnitude relation. These differences have yet to be explained, and until they are, optical and X-ray–selected cluster catalogs should be looked at as complementary, not competing.

The visually selected Abell and ACO catalogs have often been criticized for various projection effects and anisotropies. Some of these critiques have stood the test of time, while others have been found to be invalid and can be attributed to misleading conclusions and small data sets. For instance, while Sutherland (1988), Efstathiou et al. (1992), and Dalton et al. (1994a) have claimed that the Abell catalog contains significant line-of-sight anisotropies, Miller et al. (1999a), Peacock & West (1992), and PHG92 have presented strong evidence regarding the *lack* of projection effects and anisotropies when larger samples of $R \geq 1$ clusters are used. Some of the problems with previous analyses of the Abell catalog, which led to some of these conclusions, include: (1) small cluster samples ($N_{cl} \simeq 100$); (2) many cluster redshifts based on one observed galaxy; (3) cluster samples that include $R = 0$ Abell clusters that were originally cataloged by Abell in an incomplete manner. Miller, Ledlow, & Batuski (1999b) have shown that two recent X-ray cluster samples (the XBACs and the RASS1 southern cluster survey) also have line-of-sight anisotropies similar to those reported in early studies of the Abell catalog Sutherland (1988). Considering the lack of anisotropies in the $R \geq 1$ Abell cluster samples (see Miller et al. 1999a, 1999b), it remains uncertain whether X-ray surveys offer a clear advantage over optical samples. One would hope that once cluster catalogs become large enough, the statistics that describe the large-scale structure become independent of the method used to define the large-scale structure.

The MX Surveys I and II cannot directly address the question of completeness in the Abell and ACO catalogs, since we are only looking at Abell clusters (however, see Fig. 6). Large-scale galaxy surveys, such as 2dF and SDSS, will be able to definitively answer the completeness question in the future.

The MX Northern Abell Cluster Survey was undertaken in an attempt to rectify the above problems associated with the Abell sample of clusters. Our goals in this observational program were as follows:

1. Create a large sample, in both number and volume, of $R \geq 1$ three-dimensional cluster positions, in z-space, with minimal cost and observing time. We have chosen $R \geq 1$ clusters, since they make up a statistically complete sample as defined (albeit subjectively) by Abell in 1958.
2. Observe all northern hemisphere Abell $R \geq 1$ clusters to $m_{10} = 17.0$ that had not been observed before or that only had one measured galaxy redshift.
3. Observe $\simeq$20 galaxies per field using the MX multifiber spectrograph.

The observations were split up into two magnitude groups: those clusters with $m_{10} \leq 16.8$ and those with $16.9 \leq m_{10} \leq 17.0$. The first magnitude-limited sample will be referenced as the MX Survey I and was conducted over the years 1992–1996. Slinglend et al. (1998) presented galaxy redshifts and cluster mean redshifts for 96 observed Abell clusters in that survey. The second magnitude-limited survey is called the MX Survey II and was conducted over the years 1996–1999. The MX Survey II sample contains galaxy and cluster redshifts for 117 Abell clusters, which are presented in this work.

This paper is organized as follows: A description of the cluster observations and data analysis is presented in § 2. In § 3, we present a new, more accurate, m_{10}-z relation. We discuss the spatial number densities of our data set as compared with other sets of Abell clusters in § 4. In § 5, the sample sets used in the statistical analysis are defined. We discuss in § 6 the two-point correlation function and the effects of line-of-sight anisotropies. In § 7 is the summary of our findings.

2. MX SURVEY II CLUSTERS

The MX Northern Abell Cluster Survey II is a subset of richness class $R \geq 1$ Abell clusters with $16.9 \leq m_{10} \leq 17.0$, although a few dimmer clusters are also included. Our magnitude cutoff of $m_{10} \leq 17.0$ corresponds to a redshift limit of $z \simeq 0.12$ from equation (4) in § 3. This magnitude was chosen based on the fact that the instrument used to collect the redshift data, the MX Spectrometer on the Bok 2.3 m telescope, is efficiently sensitive down to approximately 1 mag fainter than 17, yielding plenty of target galaxies. Recall that our clusters are classified according to the 10th brightest galaxy in the cluster, but we observe many dimmer galaxies. Clusters observed in the MX survey were limited to $-17^\circ \leq \delta \leq 90^\circ$. Many researchers (e.g., PHG92) have observed clusters within $-27^\circ \leq \delta \leq -17^\circ$, allowing us to extend the declination limits of the entire sample to $-27^\circ \leq \delta \leq 90^\circ$. We also imposed a galactic latitude cut of $\pm 30^\circ$ to avoid galactic obscuration. Out of this sample, we measured only clusters that had zero or one measured redshift available in the literature. If a cluster had more than one measured redshift, we assumed the cluster redshift to be accurate, and we did not usually target such a cluster. In general, this may not always be a good assumption. Even if more than one galaxy has a measured redshift, there is finite probability that the galaxies are in the foreground or background group. However, because of limited observing time, we chose to accept the redshift values for clusters with two or more measured redshifts. Miller et al. (1999a) find that cluster redshifts based on only one galaxy redshift are in error by 2500 km s^{-1} or more 14% of the time. Similarly, they find that cluster redshifts are off by $\simeq$500 km s^{-1} 41% of the time when only one galaxy is used.

Throughout the duration of this survey, we have updated our redshift catalogs with current data supplied by other researchers conducting Abell/ACO cluster studies (see, e.g., PHG92; Dalton et al. 1994a; Katgert et al. 1996; Quintana

& Ramirez 1995; Struble & Rood 1999), in order to minimize duplicate observations of clusters.

2.1. *Spectroscopic Observations and the Determination of Redshifts*

2.1.1. *MX Instrumentation and Observational Setup*

Redshift data were collected using the MX Spectrometer, designed and built by Hill & Lesser (1986). It is mounted at the f/9 focus of the Bok 2.3 m telescope operated by Steward Observatory on Kitt Peak in Arizona. Thirty-two mechanical arms position 2.″0 diameter silica optic fibers in the 45′ focal plane of the telescope. Each arm carries two fibers, one for collecting galaxy spectra and the other for collecting background sky spectra. Light collected by the fibers is spread by a 400 groove mm^{-1} grating. The length of the CCD allows for $\simeq$4500 Å range with 2.7 Å $pixel^{-1}$ wavelength scale. We use the range from 3500–7100 Å. The CCD in use is a Loral 800 × 1200 pixel UV-sensitive chip. Back thinning was performed by Lesser in 1993 at Steward Observatory to achieve quantum efficiency of $\simeq$98%.

Target positions were determined from 30′ × 30′ sections of the Digitized Sky Survey[4] using code provided by Bill Oegerle and Richard White. Specifically, the algorithm centroids on the galaxy light distribution in the image and outputs the galaxy's position in α and δ to within an accuracy of 0.″3 relative to other objects in the field. This high accuracy in the object's position allows us to accurately place a 2″ fiber on each galaxy image. During this position measurement process, priorities are assigned to each target based on apparent magnitude and location with respect to the apparent center of the cluster. In other words, we intentionally target galaxies that we believe a priori to be cluster members. Approximately 30–50 galaxy positions are determined per field. The galaxies selected as targets are unmerged and bright, with a higher concentration of targets near the apparent cluster center. After galaxies are chosen and priority assigned, an IRAF routine written specifically for the MX spectrograph arranges the fiber optic probes to achieve maximum objects and maximum priority. Of the 32 object fibers on the MX Spectrograph, 25–30 are typically used during the observation. No attempt was made to have complete coverage of a particular magnitude range within a cluster.

2.1.2. *MX Observations*

The spectroscopic observations for the 117 clusters observed for the MX Survey II were taken during dark time over a period of 3 yr in 1996 February, 1996 May, 1996 October, 1997 March, 1997 October, 1998 February, 1998 November, and 1999 March. We were awarded 23 nights of dark time, 21 of which turned out to be clear. The observations generally occurred during conditions of moderate to good seeing (1″–3″).

A typical observation consists of taking the calibration and object frames. The calibration frames include fiber flats and comparison arc frames. The objects are observed over 1 hr integrations if the cluster $m_{10} \leq 17.0$. Two 45 minute integrations may be taken for some of the dimmer clusters. In the latter case, the extracted spectra are summed during reduction.

2.1.3. *Data Reduction and Spectrum Extraction*

All data reduction is done using the IRAF[5] environment. MX specific routines were developed by John Hill, Bill Oegerle, Dennis Zaritsky, and David Batuski.

First we add the bias frames together, average them, and then subtract the average frame from each object frame. We use averaged flat frames combined with the object frames to create a quotient frame that is free of effects due to the spatially variable efficiency of the CCD. After the corrections are applied to the raw image, we extract the spectra by comparing the object frame with the fiber flat. Using comparison arc frames, taken before each object integration, we correlate pixel position with wavelength. The final step before the redshifts are calculated is to subtract the sky spectra and remove cosmic rays.

A template cross-correlation technique employing the IRAF RV package is used to determine the galaxy redshifts. Spectra from 19 objects with well-known velocities make up the template set. Each observed galaxy spectrum is cross-correlated with each of the templates. The parameter r (Tonry & Davis 1979) describes the strength of each comparison, by $r = h/(\sqrt{2}\sigma)$, where h is the height of the cross-correlation peak and σ is the rms fluctuation of the antisymmetric component of the cross-correlation function (i.e., essentially the "noise" in the cross-correlation function). We also compare each spectrum with templates from eight galaxies with higher redshift than the other 19 objects. The idea is that by comparison with galaxies at a more similar redshift, it is possible to make a stronger correlation with some spectra that have relatively low signal-to-noise ratios. Errors for individual galaxy velocities is estimated using the equation $\sigma = 280/(r + 1)$ km s^{-1}, which was empirically determined for the MX spectrometer by Pinkney et al. (1993; see also Slinglend et al. 1998).

In Table 1, we present the 1542 galaxy redshifts, errors, and positions (in J2000.0) for the 117 cluster fields observed in the MX Survey II. Column (1) is the Abell/ACO number of the cluster on which the field is centered. Column (2), α, is the right ascension (J2000.0). Column (3), δ, is the declination (J2000.0). Column (4), cz, is the velocity in units of kilometers per second, as determined from cross-correlation with multiple templates. Column (5), σ, is the estimated error in velocity measurements, also in units of kilometers per second. In Figure 1, we show stripe density plots, which provide a one-dimensional view (in cz) of each observed field.

2.2. *Cluster Redshift Determinations*

Here we describe our process for obtaining mean cluster velocities and dispersions (see also Slinglend et al. 1998 for

[4] The Digitized Sky Survey plates were produced at the Space Telescope Science Institute under grant NAG W-2166. The images of these surveys are based on photographic data obtained using the Oschin Schmidt Telescope on Palomar Mountain (operated by the California Institute of Technology and Palomar Observatory) for the POSS Palomar sky survey (POSS-I). The plates were processed into a compressed digital form with the permission of these institutions. The National Geographic Society–Palomar Observatory Sky Atlas (POSS-I) was made by the California Institute of Technology with grants from the National Geographic Society.

[5] IRAF (Image Reduction and Analysis Facility) is distributed by the National Optical Astronomy Observatory, which is operated by the Association for Research in Astronomy, Inc., under cooperative agreement with the National Science Foundation.

TABLE 1
INDIVIDUAL GALAXY VELOCITIES

Abell Field (1)	α (J2000.0) (2)	δ (J2000.0) (3)	Velocity (km s^{-1}) (4)	Error (km s^{-1}) (5)
A0003	00 08 54.56	+03 50 40.6	30,462	29
	00 09 03.30	+04 06 06.9	34,583	63
	00 09 03.45	+03 59 02.3	26,526	50
	00 09 13.02	+04 06 15.4	30,099	53
	00 09 13.89	+04 07 23.4	30,430	35
	00 09 14.38	+03 51 06.7	29,396	52
	00 09 24.18	+03 56 55.6	26,630	32
	00 09 26.75	+03 59 22.9	30,300	17
	00 09 28.31	+04 07 14.5	29,960	65
	00 09 33.14	+04 00 56.1	30,848	25
	00 09 40.63	+03 51 16.7	30,690	63

NOTES.—Units of right ascension are hours, minutes, and seconds, and units of declination are degrees, arcminutes, and arcseconds. Table 1 is presented in its entirety in the electronic edition of the Astronomical Journal. A portion is shown here for guidance regarding its form and content.

more details). The first step is to apply a gap requirement, such that when ordered in *cz* space, no two sequential galaxies within a group are separated by more than 900 km s^{-1}. This separates the galaxies into group(s) with similar velocities. The mean velocity and dispersion for each group is calculated. Next, an iterative process of adding and removing members of the groups is applied. Galaxies that passed the original 900 km s^{-1} cutoff that are not within $\pm 3\,\sigma$ of the mean are excluded. Likewise, if a galaxy does not meet the original gap requirement but is within $\pm 3\,\sigma$, it is added back into the group. The mean and dispersion are calculated again, and the 3 σ rule is reapplied. Usually this process need only be done twice and never more than four times. In cases where four or fewer galaxies are measured in a particular group, a fixed maximum deviation of 1000 km s^{-1} is used to decide which galaxies are kept. The assigned value of σ is justified by Pinkney et al. (1993), who suggest that the maximum dispersion for Abell clusters is $\sigma \simeq 1200$ (Zabludoff et al. 1993).

In cases where observations produce more than one group of galaxies in a field, additional examination is required. Plots of the galaxy positions on the sky relative to the Abell cluster center are made. These are used to determine which group is the cluster and which group(s) may be foreground or background. For an earlier comparison of MX I versus cluster velocity dispersions, see Slinglend et al. (1998).

In Table 2, we present cluster redshifts for all Abell clusters observed in the MX Surveys I and II, as well as redshifts from the literature for clusters within $z = 0.14$. For the purposes of publishing the largest and most complete $R \geq 1$ cluster sample, we also list ACO clusters in the southern hemisphere. There are a total of 669 clusters in Table 2. Of these, 213 clusters were measured by the MX surveys I and II. The 117 MX Survey II cluster redshifts appear for the first time in this work. We note that the MX surveys determined that seven clusters are not true clusters and an additional 11 clusters will require

TABLE 2
ABELL/ACO CLUSTER VELOCITIES

Cluster (1)	Reference (2)	m_{10}[a] (3)	BM Class[b] (I, II, III) (4)	μ (km s^{-1}) (5)	σ[c] (km s^{-1}) (6)	N_{cl} (7)	Notes[d] (8)
A0001	2	17.1	III	37,470	...	1	
A0002	5	17.3	II	36,810	...	1	
A0003	14	17.0	II	30,315	459	8	
A0012	2	17.2	III	37,650	...	1	
A0013	4	16.6	II	28,290	970	37	
A0016	14	17.0	III	25,120	232	7	*
A0017	5	17.6	I–II	26,640	...	1	
A0021	3	16.2	I	28,380	680	11	
A0022	3	17.5	...	42,300	...	3	
A0024	3	17.5	III	40,140	...	1	
A0034	5	18.0	I–II	39,480	...	>0	
A0038	5	17.6	II	42,420	...	1	

NOTES.—Table 2 is presented in its entirety in the electronic edition of the Astronomical Journal. A portion is shown here for guidance regarding its form and content.

[a] As determined by Abell 1958 or ACO (Abell et al. 1989). Note that there is a significant difference between the two in the way m_{10} values were assigned.

[b] Classification of Abell clusters were carried out by Leir & van den Bergh 1977 and Abell et al. 1989 and references therein. (I) Cluster contains a centrally located cD galaxy; (II) cluster where the brightest galaxy is intermediate in appearance between a cD and the Virgo-type giant elliptical galaxies; (III) cluster contains no dominant galaxies.

[c] Where available. For clusters in the MX Survey, this dispersion is only calculated when five or more galaxies were used to determine the published redshift (i.e., the dispersion is calculated from the biweight estimate of the scale Beers et al. 1990). The dispersions are in the rest frame of the cluster.

[d] An asterisk (*) refers to clusters with additional information listed in Table 3.

REFERENCES.—(1) Abell et al. 1989; (2) Struble & Rood 1999; (3) Struble & Rood 1991; (4) Katgert et al. 1996; (5) Quintana & Ramirez 1995; (6) Quintana et al. 1997; (7) van Kampen & Rhee 1990; (8) Kim et al. 1994; (9) Dalton et al. 1994b; (10) Batuski et al. 1999; (11) Zabludoff et al. 1993; (12) Huchra et al. 1990; (13) Slinglend et al. 1998; (14) new data presented in this paper.

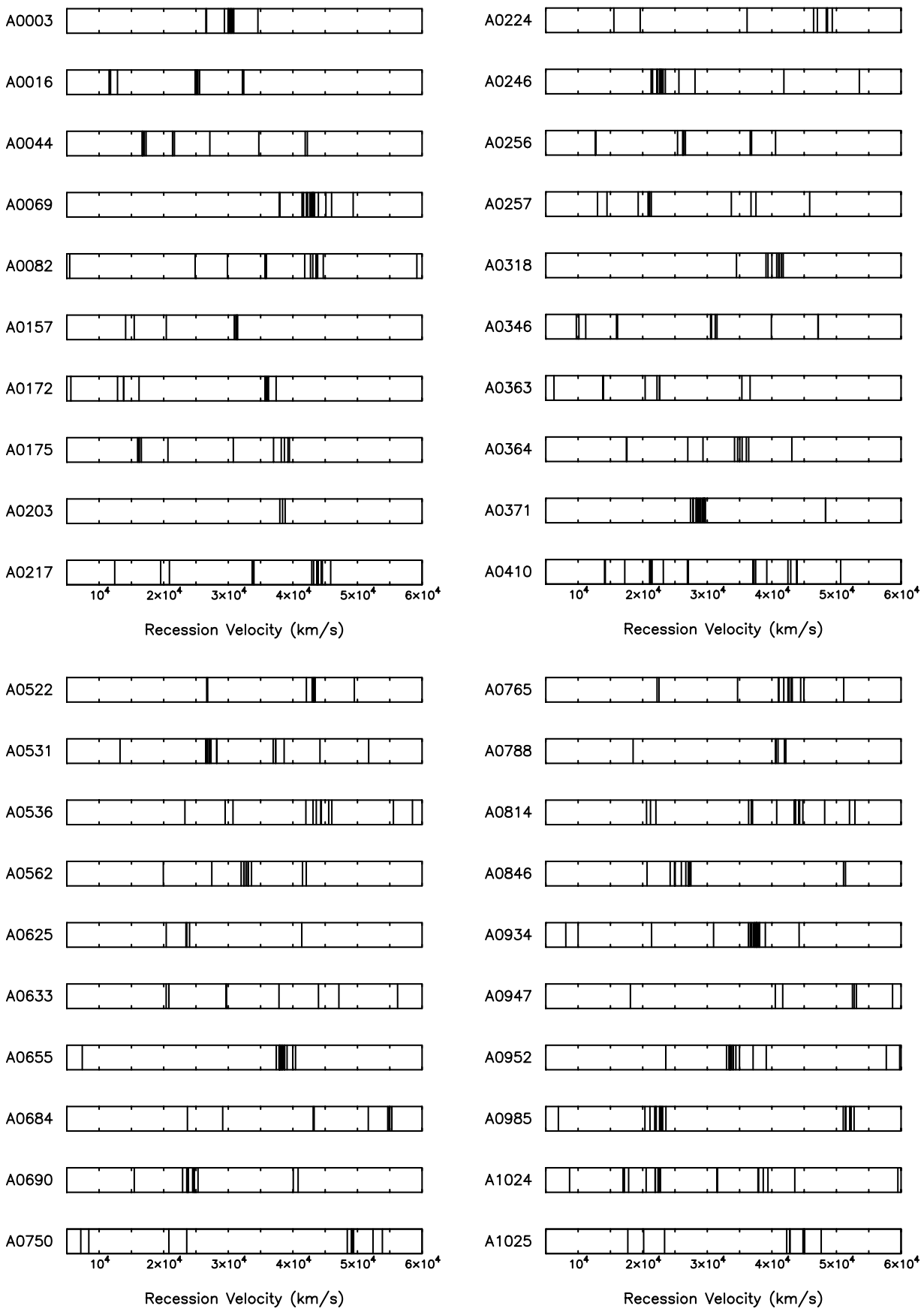

FIG. 1.—Each stripe is a galaxy within the cluster field

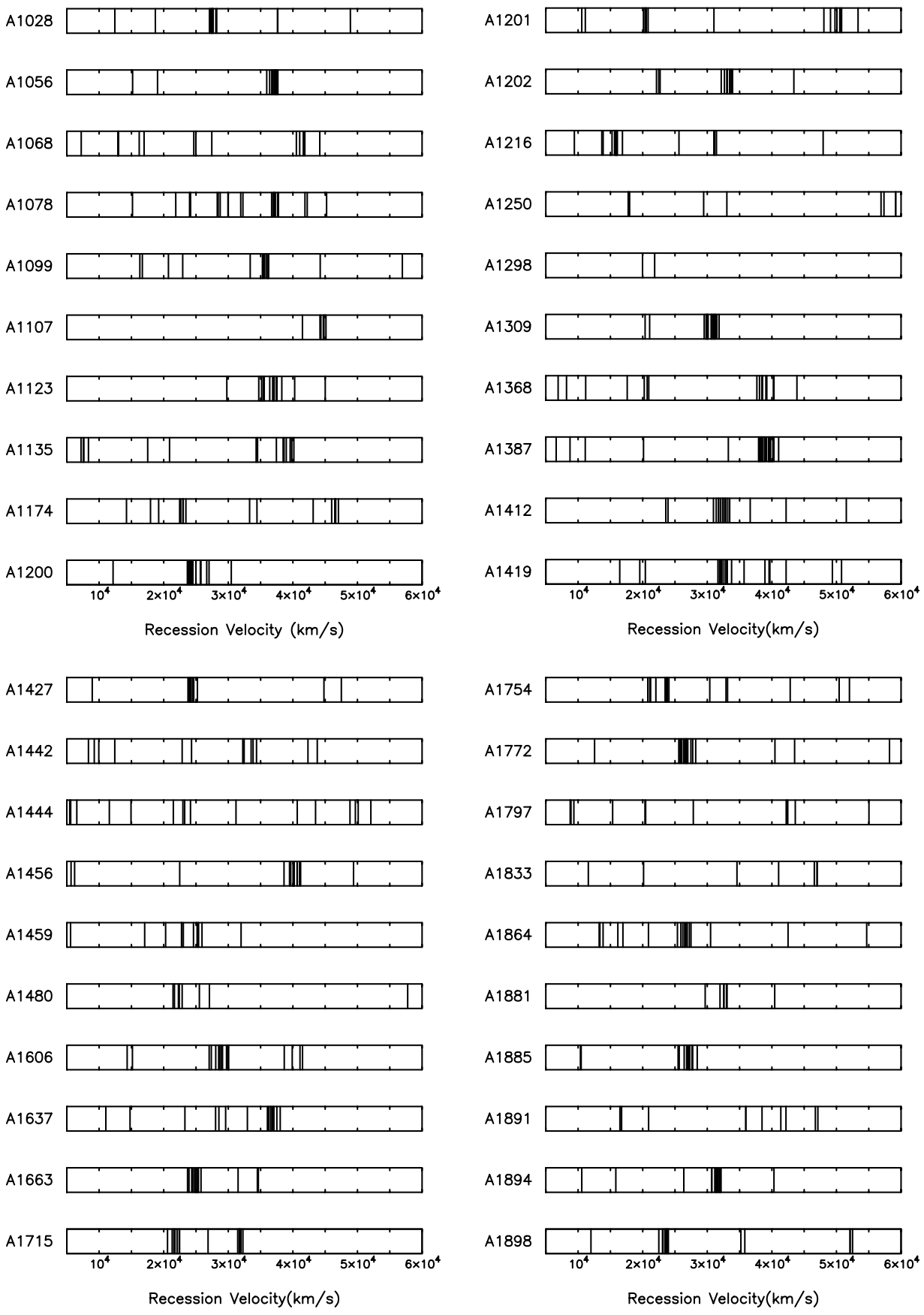

FIG. 1.—*Continued*

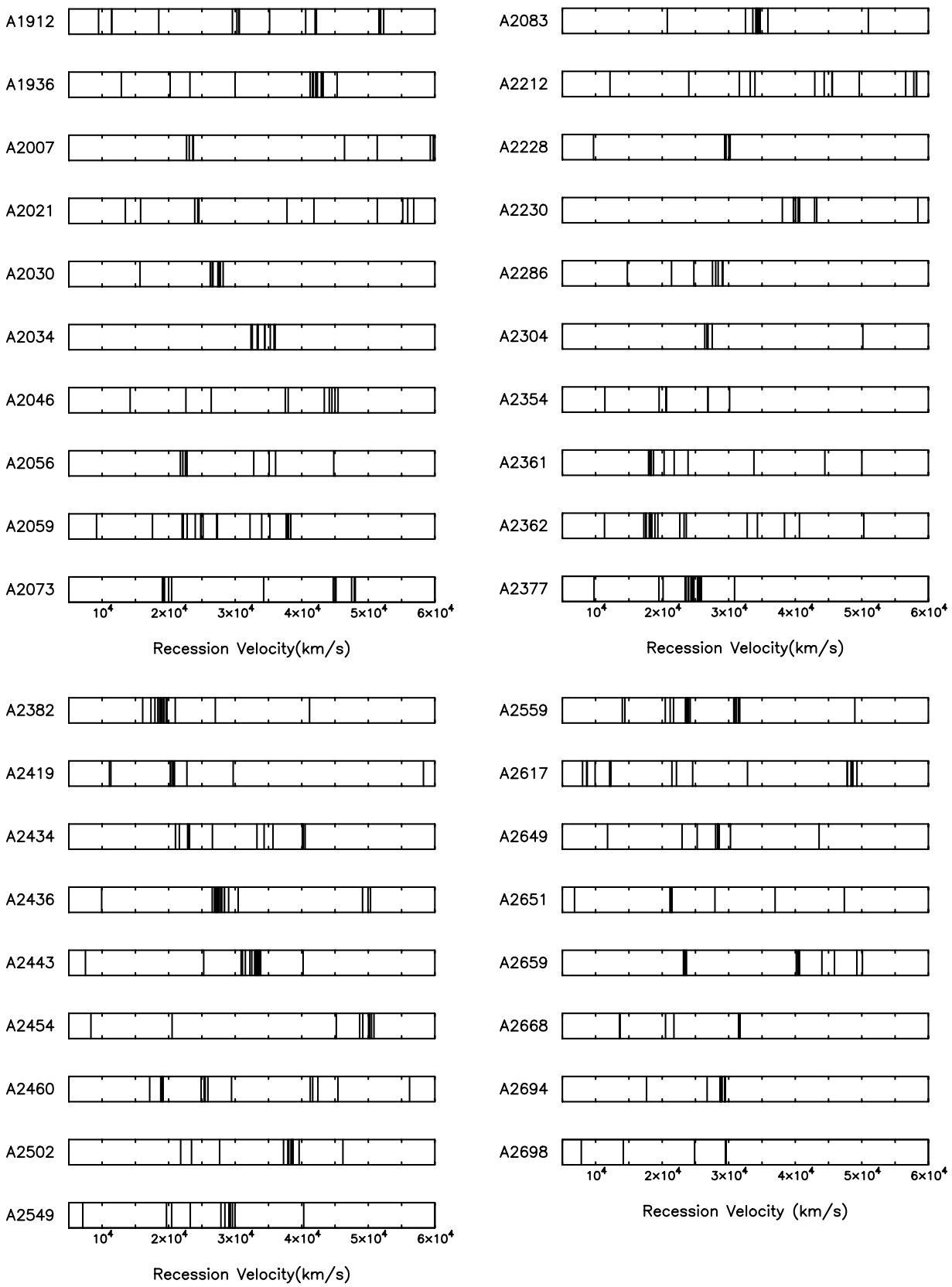

FIG. 1.—*Continued*

further spectroscopic observations for average velocity determinations.

Column (1) is the Abell/ACO cluster number.

Column (2) provides the reference for the cluster redshift and/or velocity dispersion. Except for the new cluster redshifts presented in this paper, most of the data in Table 2 can be found in a recent compilation by Struble & Rood (1999). Struble & Rood (1999) also provide references for all of the cluster redshifts and velocity dispersions listed in their compilation. Specific references can be found at the end of this table.

Column (3), m_{10}, lists the magnitude of the 10th brightest galaxy in the cluster as determined by Abell (1958) or ACO (Abell, Corwin, & Olowin 1989). Note that there is a significant difference between the two in the way m_{10} values were assigned.

Column (4), *BM*, indicates the cluster Bautz-Morgan class (for a definition, see Bautz & Morgan 1970). Class I clusters contain a centrally located cD galaxy. Class II identifies clusters where the brightest galaxy is intermediate in appearance between a cD and the Virgo-type giant elliptical galaxies. Class III clusters contain no dominant galaxies. Classification of Abell clusters were carried out by Leir & van den Bergh (1977) and Abell et al. (1989) and references therein.

Column (5), μ, lists the mean velocity of the galaxies within each cluster. If more than four galaxy redshifts were available in MX Survey clusters, the biweight location estimator (Beers, Flynn, & Gebhardt 1990) was used. However, not all of the other cluster redshifts in Table 2 were determined using the biweight location estimator. In fact, it is not always clear what method has been used by other researchers for the calculation of the mean. Still, the value presented in column (5) is the best velocity available for use in the determination of the radial distance to the center of each cluster.

Column (6), σ_v, is the cluster velocity dispersion, where available. For clusters in the MX Survey, this dispersion is only calculated when five or more galaxies were used to determine the published redshift (i.e., the dispersion is calculated from the biweight estimate of scale; Beers et al. 1990). The dispersions are in the rest frame of the cluster.

TABLE 3
MX Survey II Cluster Notes

Cluster	Notes
A0016	Background clump northeast of cluster center. $N_{gr} = 3$ and $cz \sim 32{,}000$ km s^{-1}.
A0044	No obvious cluster. There are four galaxies very near cataloged center: two at $cz \sim 41{,}500$ km s^{-1}and two at $cz \sim 21{,}000$ km s^{-1}.
A0069	There is also a pair of galaxies at $cz \sim 37{,}000$ km s^{-1}, very near the cataloged center.
A0082	There is a foreground group of $N_{gr} = 3$ and $cz \sim 36{,}000$ km s^{-1}.
A0175	There is a foreground group of $N_{gr} = 4$ and $cz \sim 16{,}000$ km s^{-1} east of center.

Notes.—Table 3 is presented in its entirety in the electronic edition of the Astronomical Journal. A portion is shown here for guidance regarding its form and content.

Column (7), N_{cl}, is the number of galaxy velocities within each group that went into each mean and dispersion calculation.

Column (8) indicates any notes for clusters observed via the MX Survey II. Each note is described in Table 3. We point out that many of the clusters not observed in the MX Survey also have notes listed in Struble & Rood (1991; 1999).

Cluster velocities that are specified with an "N/A" do not have enough measured galaxies for a clear determination. Ones that are specified with an "N/C" do not appear to be clusters at all, but simply many galaxies (i.e., 15 or so observed) along the line of sight.

The MX Surveys I and II (or collectively the MX Survey) have helped increase the latitude-limited ($\delta \geq -27^\circ$ and $|b| \geq 30^\circ$), magnitude-limited (to $m_{10} = 17.0$) sample size from 126 (PHG92) clusters to 350 clusters. At the same time, we have reduced cluster redshift uncertainties, since of the 350 clusters with at least one member galaxy with measured redshift, 321 now have two or more measured cluster members, while 232 have five or more. The MX Surveys I and II have obtained an average of eight cluster member redshifts in 195 of the clusters targeted for this survey. For those clusters with eight or more member redshifts, we can calculate velocity dispersions to be used in future studies of luminosity functions, mass functions, and other properties of clusters.

3. $m_{10} - z$ RELATION

The relationship between the apparent magnitude of the 10th brightest galaxy in a cluster and the cluster's redshift is a commonly used tool for estimating the distance to clusters with unknown redshift. Abell (1958) used such an estimator for the redshift values in his original catalog. Postman et al. (1985) recalculated the magnitude-redshift relation with clusters using known redshifts, but $R = 0$ clusters and clusters with only one measured redshift were used. While our goal was to measure redshifts for all Abell/ACO clusters within $z \simeq 0.1$, an updated m_{10}-z relation might prove useful for clusters between $0.1 \leq z \leq 0.15$, where it is known that most $R \geq 1$ Abell/ACO-type clusters were, in fact, cataloged, but many are still not observed because of our survey limits (see Ebeling et al. 1996 and references therein).

We use the data set of measured Abell clusters in the northern hemisphere to fit the magnitude-redshift relation. Only $R \geq 1$ clusters with two or more measured redshifts are used. The declination cut is at $\delta = -27^\circ$. The galactic latitude cut was made at $|b| \geq 27^\circ$. We also apply a magnitude constraint from $14.8 \leq m'_{10} \leq 18.0$, where m'_{10} is the adjusted 10th brightest galaxy magnitude as described below.

First, we correct for the brightening of the observed spectrum because of the finite width of the filter used in a given observation. Because redshift is a function of wavelength with long wavelengths shifted less than short wavelengths, a filter allows more photons to pass through if the spectrum is redshifted than if the filter was in the rest frame of the source. The shape of the spectrum also plays a role in the dependence of brightness on redshift, but we do not take this into account. Our *K*-correction is of the form $K = 2.5 \log (1 + z)$ (Oke & Sandage 1968). Next, we correct

TABLE 4
MX Survey II Average Absolue Magnitudes

Richness	$\langle M_{10} \rangle$	$\Delta m_{\rm Scott}$	Number of Clusters
1.....	−20.60	0.00	572
2.....	−20.83	0.23	251
3.....	−21.03	0.43	67
4.....	−21.14	0.54	7

for dimming due to dust and neutral hydrogen in our own Galaxy using the Schlegel, Finkbeiner, & Davis (1998) maps of column density across the sky.

The corrected form of the magnitude is

$$m_{10,c} = m_{10,\rm Abell} + K - m_{10,\rm ext} \quad (1)$$

where $m_{10,c}$ is the corrected magnitude, $m_{10,\rm Abell}$ is Abell's designated m_{10}, K is the K-correction term, and $m_{10,\rm ext}$ is the extinction correction.

Finally, after the m_{10} is corrected for observational biases, the Scott correction is applied (Scott 1957) to account for a selection bias that can skew the m_{10}-z relation. This bias occurs at the edges of the survey. Nearby, we find more intrinsically dim poor clusters. While at higher redshifts, we find more intrinsically bright rich clusters. Therefore, we must calibrate the magnitudes of each richness class relative to $R = 1$ to remove this bias. Table 4 lists values of the average absolute magnitude of the 10th brightest galaxies for the four richness classes.

The final form of the adjusted magnitude for use in the m_{10}-z relation is

$$m'_{10} = m_{10,c} + \Delta m_{\rm Scott} \ , \quad (2)$$

where $\Delta m_{\rm Scott} = \langle M_{10} \rangle_{R=1} - \langle M_{10} \rangle_{R=N}$.

Figure 2 shows the Hubble diagram of our data set using equation (2). The solid line is the best-fit linear curve through the data. Fitting was accomplished using a robust line-fitting technique (see, e.g., Press, Rybicki, & Hewitt 1992). The best-fit line equation is

$$\log z = (0.2121 \pm 0.0076) m'_{10} - 4.539 \pm 0.032. \quad (3)$$

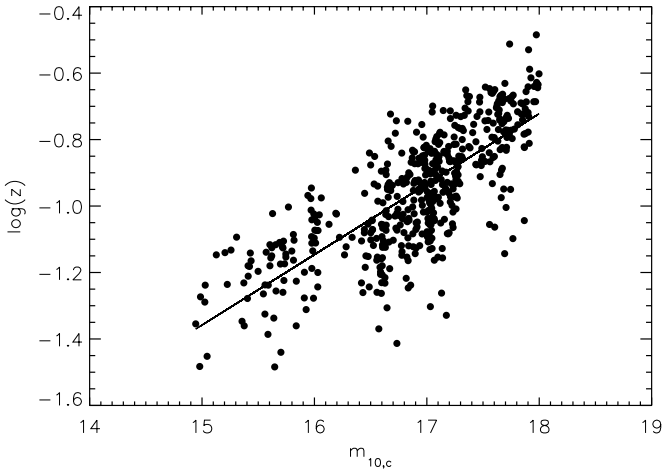

FIG. 2.—Magnitude-redshift relation for $R \geq 1$ Abell clusters having two or more measured galaxy redshifts in the corrected magnitude range $14.8 < m'_{10} < 18.0$.

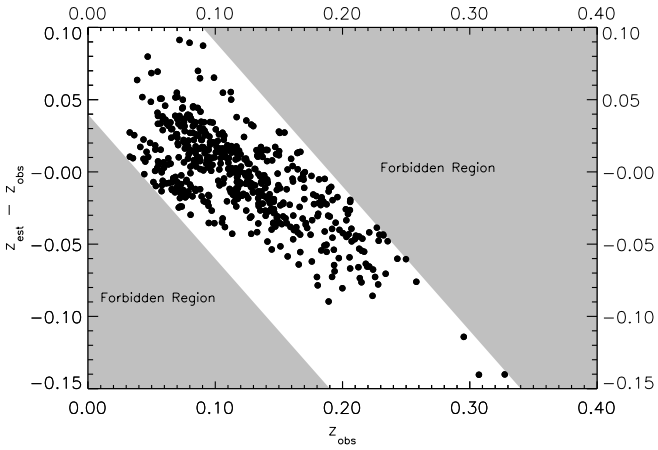

FIG. 3.—Dispersion on our magnitude redshift relation. The "forbidden" regions are a result of the magnitude cuts at $m'_{10} = 14.8$ and 17.0.

Our fit has a slightly steeper slope than that found by Postman et al. (1985). The forbidden regions in Figure 3 contain no data because of our upper and lower magnitude cuts. There are a few outliers that, in the past, have been assumed to be a result of foreground or background contamination. We have virtually eliminated this possibility by using clusters that have two or more measured redshifts. Although there is a chance that two measured redshifts could both be foreground and background, it is more likely that the outliers are due to deviant m_{10} estimations.

The overall dispersion of the estimator in $\log z$ is $\sigma = 0.0256$. For the $n \geq 1$ case, σ increases by 16%. One can see that the way points are arranged on the redshift residual plot is greatly affected by the "forbidden" regions. At approximately $z = 0.2$ all plotted points are negative. Similarly, at $z = 0.04$, the points are positive. This confines the estimator to a range of values $0.1 < z < 0.15$, where we see the best performance. Because our catalog of measured redshifts is complete to $z = 0.1$, we need not estimate at lower redshifts. The estimator can be used at redshifts higher than 0.15; however, it must be noted that the evaluation of the performance of the estimator becomes difficult for $z > 0.15$.

4. THE SPATIAL NUMBER DENSITY OF $R \geq 1$ ABELL CLUSTERS

The number density in a proper volume, $n_p(z)$, of a survey can be calculated for a Friedmann universe (Narlikar 1983):

$$dn_o = d\Omega \left(\frac{c}{H_0} \right)^3 \frac{\{q_o z + (q_0 - 1)[(1 + 2zq_0)^{1/2} - 1]\}^2 n_p \, dz}{q_0^4 (1+z)^6 (1 + 2q_0 z)^{1/2}} \ , \quad (4)$$

and we have (e.g., Miller et al. 1999a)

$$dn_o = d\Omega \left(\frac{c}{H_0} \right)^3 \frac{z^2 (2+z)^2 n_p \, dz}{4(1+z)^6} \quad (5)$$

for $q_0 = 0$, where dn_o is the number of observed clusters within dz, and $d\Omega$ is the solid angle subtended by the survey.

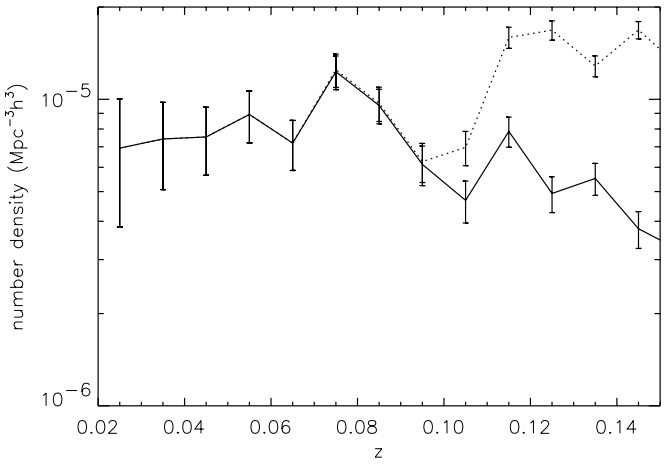

FIG. 4.—Density of Abell clusters with $R \geq 1$. The solid line is for clusters with measured redshifts. The dotted line includes clusters with estimated redshifts when no published cluster redshift is available.

If we include an unknown selection function in z, $S(z)$, and the evolution of n_p via $E(z)$, we must let $n_p(z) \rightarrow n_p(z)S(z)E(z)$ (Kolb & Turner 1990). For the samples mentioned above, we assume $E(z) = S(z) = 1$ for simplicity, since evolution of the proper number density of clusters should be negligible at these low redshifts, and we are only studying a volume that has a nearly constant density (see Fig. 4), making $S(z) \simeq 1$.

First, we will examine the number density of Abell (1958) clusters in the northern hemisphere (i.e., $\delta \geq -27°$). In Figure 4, we plot the proper number density for clusters with measured redshifts (*solid line*). We also plot the number density using equation (3) to estimate the redshifts for those clusters that currently have no observations (*dotted line*). Note that the corrected m_{10} is used in equation (3), which contains K as a function of z. We perform an iterative technique to find the final estimated redshift (Postman et al. 1985). Figure 4 shows our sample contains almost all rich Abell clusters to $z = 0.10$.

In Figure 5, we plot the number densities of northern Abell cluster samples (having measured redshifts) using an increasing m_{10} cutoff. At each increment, the falloff in the density occurs at a higher redshift, while the density at low redshifts remains essentially constant. Because adding dimmer clusters should add higher redshift clusters to the set, we expect the low-redshift density to be undisturbed by a higher m_{10} cutoff. This plot also gives the reader an understanding of how incomplete earlier cluster samples have been. For instance, consider the $m_{10} \leq 16.5$ samples of Bahcall & Soniera (1983) and PHG92. From Figure 5, we see that this magnitude subset of Abell clusters becomes significantly incomplete at $z \simeq 0.05$. With our newly enlarged cluster data set, the difference in the number density between samples with $m_{10} \leq 17.2$ and with no limit is small out to a redshift of $z \simeq 0.10$. Coupled with the negligible difference in the estimated versus real density out to $z = 0.10$ in Figure 4, it is evident that our sample is volume-limited and essentially complete (to the limiting magnitude of the Abell catalog) to $z = 0.10$.

Finally, we compare the number density of clusters in the northern Abell sample with the southern ACO sample (see Fig. 6). Miller et al. (1999a) found a higher mean density for the ACO southern set of clusters compared with the Abell northern set, supporting previous claims that the ACO clusters are slightly poorer than their northern counterparts. In addition, a study of the X-ray luminosity functions of Abell versus ACO clusters suggests that $R \geq 2$ ACO clusters are equivalent to $R \geq 1$ Abell clusters (Jones & Forman 1999). Therefore, as in Miller et al. (1999a), to achieve similar densities in the north and south, we excluded those clusters with $N_{\rm gal} \leq 60$, where $N_{\rm gal}$ is the number of galaxies within an Abell radius as listed in the ACO catalog, resulting in exclusion of 36 of the poorest ACO $R = 1$ clusters. The area surveyed by the northern Abell sample is significantly larger than that in the southern set (4.83 sr vs. 1.45 sr). Therefore, the errors and scatter on the density are larger for the southern data. In Figure 6, we see that both volumes have nearly identical number densities out to $z = 0.1$, with

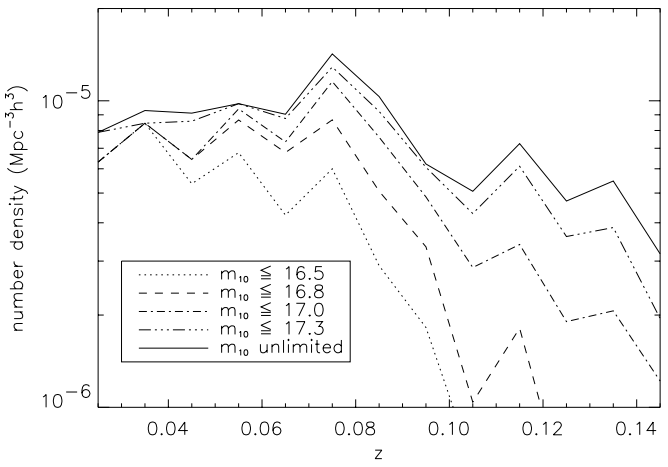

FIG. 5.—Same as Fig. 4, but for various limiting m_{10} values. Notice that the number densities for our magnitude limit ($m_{10} = 17.0$) are similar to the unlimited sample out to $z = 0.10$, indicating that adding higher magnitude clusters will not significantly enlarge our $z \leq 0.10$ volume-limited sample.

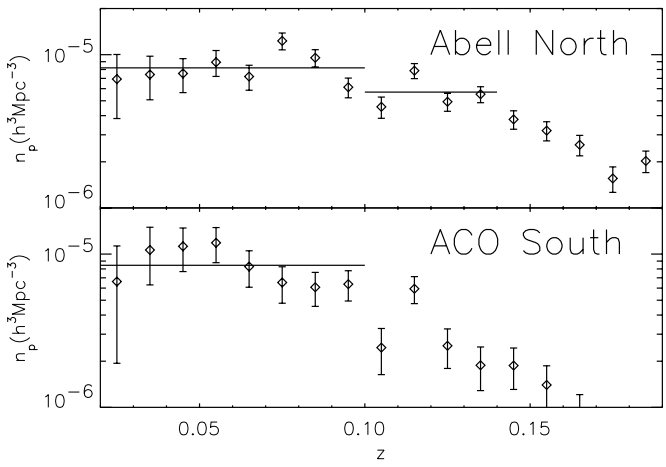

FIG. 6.—Number densities of northern and southern clusters. *Top*: Number density in the northern hemisphere ($-27° \leq \delta \leq 90°$). This northern sample contains all measured $R \geq 1$ Abell (1958) clusters within $z = 0.14$. *Bottom*: Number density, n_c, for the southern hemisphere ACO (Abell et al. 1989) $R \geq 1$ clusters with $N_{\rm gal} > 60$. This sample contains all measured clusters within $z = 0.10$. The solid lines are the average number densities as defined in the text.

$n_{\rm north} = 8.25 \pm 1.9 \times 10^{-6}$ h^3 Mpc^{-3} and $n_{\rm south} = 8.45 \pm 2.4 \times 10^{-6}$ h^3 Mpc^{-3} after excluding the poorest ACO clusters (with $N_{\rm gal} < 60$). In the north, the density of clusters with measured redshifts then drops to $5.72 \pm 1.4 \times 10^{-6}$ h^3 Mpc^{-3} for $0.1 < z \leq 0.14$. For comparison, the spatial number density of APM clusters is 3 times as large at $\simeq 2.4 \times 10^{-5}$ h^3 Mpc^{-3} (Dalton et al. 1994b). Our number density is most similar to the $R = 70$ clusters from Croft et al. (1997).

5. CLUSTER SAMPLES

The addition of the MX Survey clusters to ones previously cataloged by other researchers brings the total number of observed clusters with $m_{10} \leq 17.0$, $R \geq 1$, and $-27^\circ \leq \delta \leq 90^\circ$ to 350 out of 368 listed in the Abell (1958) catalog. Figure 7 shows how much improved the MX survey is compared with earlier surveys. The histograms are of the compiled cluster redshifts presented in this paper compared with the compilation done by Struble & Rood (1991), both with the limits stated above. Notice the relatively flat distribution of percentage of clusters measured out to 12 measured member galaxies. A survey in the southern hemisphere, the ESO Nearby Abell Cluster Survey (ENACS) has added redshifts for 104 $R \geq 1$ ACO clusters with mean redshifts $z \leq 0.1$ (Katgert et al. 1996). The depth of the ENACS survey is similar to the MX survey and thus provides an excellent southern data set that can be combined with the MX survey for all-sky studies. We note that there are differences between $R \geq 1$ Abell clusters and $R \geq 1$ ACO clusters (e.g., Batuski et al. 1989 and references therein). Such differences between the catalogs include V- versus R-band magnitude determinations (ACO and Abell, respectively), greater sensitivity of the IIIa-J plates used in the ACO catalog, and a global determination of the background galaxy count versus local determinations (ACO and Abell, respectively). However, we show in § 6 that differences in the Abell/ACO galaxy member counts make little difference in the measurement of the correlation function. Below, we discuss the subsets of clusters we use in the spatial analyses.

Sample 1: The whole-sky statistical sample.—Contains the 257 $R \geq 1$ Abell clusters in the northern hemisphere plus 81 $R \geq 1$ ACO clusters with $-90^\circ \leq \delta \leq -27^\circ$, $0^{\rm h} \leq \alpha \leq 24^{\rm h}$. We note that ACO examined the region $-17^\circ \leq \delta \leq -27^\circ$, as did Abell (1958). In many cases, ACO found the same clusters as Abell; however, a few new clusters were also found and in some other clusters the richness classification was altered. We include seven "overlap" clusters in our sample and use the richnesses as specified in ACO. All of the clusters in this sample are within $z = 0.10$ (or 286 h^{-1} Mpc). The number density for this sample is constant and well defined to $z = 0.10$ with a total of 338 clusters.

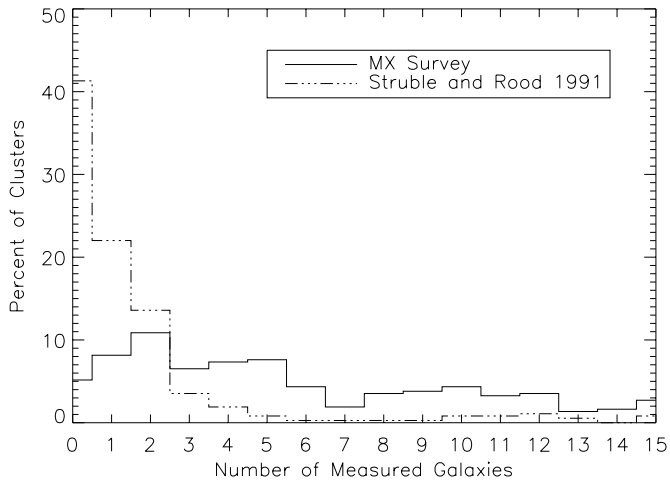

FIG. 7.—Comparison of the compilation of measured Abell cluster redshifts by Struble & Rood (1991) with the compilation presented in this paper. Both sets contain 368 clusters.

Sample 2: The whole-sky volume-limited sample.—Notice in Figure 6 that the density only drops from 8.25×10^{-6} to 5.72×10^{-6} h^3 Mpc^{-3} from $z = 0.10$ out to $z = 0.14$. Using all possible cluster redshifts from Table 2 (i.e., no magnitude limit) we have created a sample of 598 $R \geq 1$ Abell/ACO clusters with $|b| \geq 30^\circ$. We exclude any cluster beyond $z = 0.10$ in the south ($\delta \leq -27^\circ$) and beyond $z = 0.14$ in the north ($\delta \geq -27^\circ$) for completeness reasons (Miller et al. 1999a). Only $\simeq$20% of our cluster redshifts are based on one measured redshift. This is the largest cluster sample compiled to date for large-scale structure analyses. The survey volume covers 1.2×10^8 h^{-3} Mpc^3 and is nearly 4 times larger than the volumes covered by the APM cluster survey (Dalton et al. 1994b) and the Retzlaff et al. (1998) Abell/ACO survey.

6. TWO-POINT SPATIAL CORRELATION FUNCTION

The two-point spatial correlation function is used to describe the scale of clustering within discrete data sets. Both galaxies and clusters of galaxies have a functional power-law form for the correlation function $\xi(r) = (r/r_o)^\gamma$. The amplitude and slope of this power law are rather well defined for galaxies to be $r_o = 5$ h^{-1} Mpc and $\gamma = -1.8$ (e.g., Willmer, Da Costa, & Pellegrini 1998 and references therein). For galaxy clusters, the slope has been established at $-2.0 \leq \gamma \leq -1.8$, but the value for r_o has been a matter of much debate. The majority of cluster-cluster spatial correlation analyses have been based on the visually "scanned" Abell and ACO catalogs (Abell 1958; Abell et al. 1989) and the machine scanned APM cluster survey (Efstathiou et al. 1992; Dalton et al. 1994a, Croft et al. 1997). The correlation length for the visually selected clusters is $\sim$20–25 h^{-1} Mpc with positive correlations out to separations of $\sim$50 h^{-1} Mpc (e.g., Miller et al. 1999a and references therein). However, the clusters selected through machine scanning have $r_o \sim 15$ h^{-1} Mpc and little positive correlation beyond 25 h^{-1} Mpc (Efstathiou et al. 1992; Dalton et al. 1994b).

There have been similar disparities in X-ray–selected samples. For instance, the XBACs and the RASS1 cluster surveys find $21 \leq r_o \leq 26$ h^{-1} Mpc (Abadi, Lambas, & Muriel 1998; Moscardini et al. 2000; Borgani, Plionis, & Kolokotronis 1999). While the earlier works of Nichol, Briel, & Henry (1994) and Romer et al. (1994) find $r_o \leq 16$ h^{-1} Mpc. These large differences between the above determinations of r_o for clusters have been explained in either of two ways:

1. Cluster catalogs, either optical or X-ray, suffer from spurious cluster selection. This observational selection bias occurs when two clusters are near each other on the plane of the sky, but separated by a large distance radially. When this occurs, the richness of either the foreground or back-

ground cluster may be artificially enhanced because of projection effects. (e.g., Sutherland 1988; Efstathiou et al. 1992). We point out that a substantial number of clusters missed in a nonrandom systematic matter during the visual selection process can also give rise to this effect (i.e., plate-to-plate magnitude differences or human failings; see, e.g., Dalton et al. 1992 for more details).

2. The value of r_o is dependent on the mean cluster number density (n_c) of the sample,

$$r_o = 0.4 n_c^{-1/3} . \quad (6)$$

In this case, the APM clusters should have a smaller correlation length, since their number density is nearly 4 times that of $R \geq 1$ Abell clusters (Bahcall & West 1992; Bahcall & Cen 1994).

While both of the above solutions seem plausible and explain (and/or correct) the value of r_o, both solutions have also been shown to be flawed. Line-of-sight anisotropies within the Abell and ACO catalogs have been examined in detail by Miller et al. (1999a), who find that only $\sim$10% of clusters in the ENACS (Katgert et al. 1996) and MX (Slinglend et al. 1998) surveys show strong background and/or foreground contaminations. In addition, Miller et al. find $r_o \sim 20\ h^{-1}$ Mpc for $R \geq 1$ Abell clusters both before and after removing these contaminated clusters from the analysis. They also show that the minimal anisotropy present in the $R \geq 1$ subset of clusters is similar in scale to that of the APM clusters. Miller et al. conclude that projection effects and line-of-sight anisotropy are not serious problems for $R \geq 1$ Abell/ACO clusters and do not artificially enhance r_o.

On the other hand, the density dependence on the correlation length was determined empirically and ultimately depends on the accurate evaluation of r_o and the mean cluster density for multiple samples. While many of the currently available cluster data sets have mean densities $\sim 1 \times 10^{-5}\ h^3$ Mpc^{-3} or greater, until recently, only the richest ($R \geq 1$) Abell clusters have provided r_o for data sets with densities $\sim 1 \times 10^{-6}\ h^3$ Mpc^{-3}. Croft et al. (1997) constructed a catalog of very rich APM clusters with a mean number density of $\sim 1 \times 10^{-6}\ h^3$ Mpc^{-3} and find $r_o = 21\ h^{-1}$ Mpc, which is contrary to the expected result from equation (1). Using N-body simulations, both Croft & Efstathiou (1994) and Eke et al. (1996) find that the density dependence on the correlation length is much weaker than in equation (6) for APM clusters and ΛCDM models. Unfortunately, we do not have a statistically significant determination of r_o for $R \geq 2$ Abell clusters (with $\bar{n} \sim 1 \times 10^{-6}\ h^3$ Mpc^{-3}), although results from Peacock & West (1992) and Postman, Huchra, & Geller (1986) suggest that the correlation length may be as high as $r_o = 45\ h^{-1}$ Mpc. With only two very rich samples studied so far, equation (6) lacks strong observational support for densities less than $10^{-5}\ h^3$ Mpc^{-3}.

The study of large-scale structure in the universe plays a vital role in the determination of the cosmological parameters and scenarios that describe the universe from just after its creation to what we see today. It is the visible structure on scales greater than $\simeq 50\ h^{-1}$ Mpc that can tell us directly about the nature of the initial conditions that could have generated such large-scale structures. In this section, we will examine the two-point spatial correlation function to help us quantify structures on large scales. Many authors have performed similar analyses on Abell clusters (e.g., Bahcall & Soniera 1983; West & van der Bergh 1991; PHG92; Jing, Plionis, & Valdarnini 1992; Peacock & West 1992; Abadi et al. 1998; Miller et al. 1999a). The largest $R \geq 1$ Abell cluster sample examined before this work included only 289 Abell/ACO clusters (Miller et al. 1999a). With the addition of MX Survey II clusters (as well as other redshifts from the literature), we can examine a cluster data set that is more than twice as large as the Miller et al. (1999a) sample, and 6 times as large as the Bahcall & Soniera (1983) sample of 104 $R \geq 1$ Abell clusters.

We use the following estimator derived in Hamilton (1993) for the determination of the correlation function:

$$\xi(r) = \frac{\mathrm{DD}(r) \times \mathrm{RR}(r)}{\mathrm{DR}(r)^2} - 1 , \quad (7)$$

where DD, RR, and DR are the data-data, random-random, and data-random pair counts, respectively, with separations between $r - (\Delta r/2)$ and $r + (\Delta r/2)$. Compared with previous estimators (see Bahcall & Soniera 1983 and PHG92), this one is proposed to be less affected by uncertainties in the mean number density where separations are large and ξ is small. Ratcliffe et al. (1998) used N-body simulations to show that equation (6) provided the most accurate results when compared with other estimators.

The random pair counts (DR, RR) are evaluated by averaging over 200 Poisson distributed catalogs generated with the same number of pseudoclusters as the sample under consideration. The angular coordinates in these catalogs are randomly assigned with the same boundary conditions as the survey. In most two-point function analyses, a galactic latitude selection function, $P(b) = 10^{\alpha(1 - \csc |b|)}$, with $\alpha \simeq 0.32$ is imposed to account for residual galactic obscuration (See PHG92 and Peacock & West 1992 for

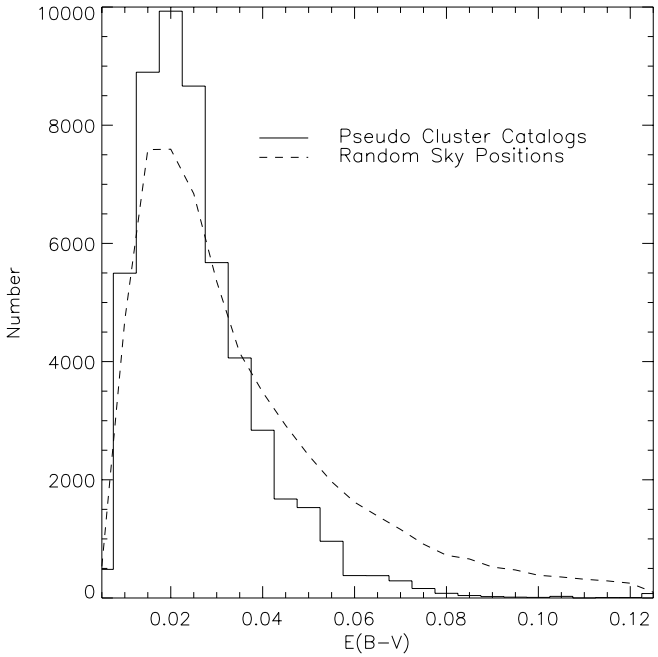

FIG. 8.—Distribution of extinction values as taken from the Schlegel et al. (1998) maps. We compare the distribution of our pseudocluster catalogs (which have the same distribution as our real cluster samples) with randomly selected positions.

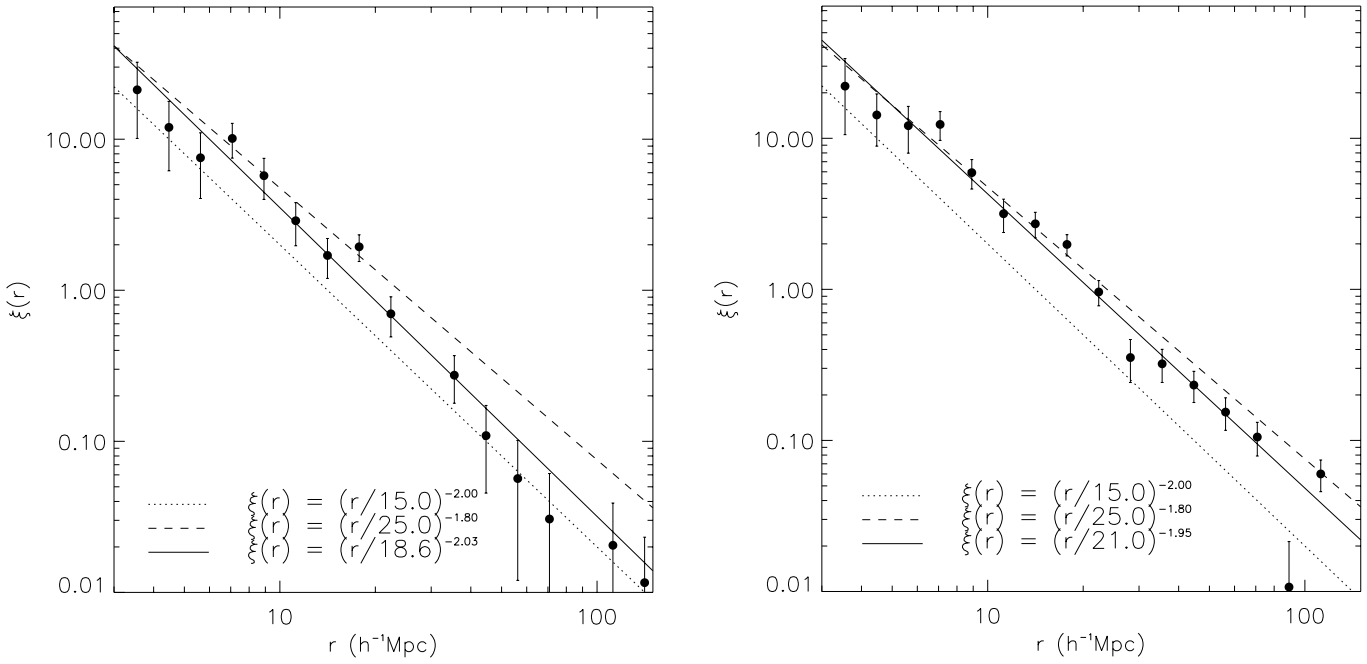

FIG. 9.—*Left*: Two-point spatial correlation function for the whole-sky, volume-limited sample (to $z = 0.10$) (sample 1). *Right*: Two-point spatial correlation function for the whole-sky volume-limited sample (to $z = 0.10$ in the south and to $z = 0.14$ in the north) (sample 2). In both plots, the dashed line represents the early power-law fits of ξ for Abell clusters (e.g., Bahcall & Soniera 1983), and the dotted line corresponds to the APM cluster results (e.g., Efstathiou et al. 1992).

examples.). However, with the release of the Schlegel et al. (1998) H I extinction maps, we can create random catalogs with the same extinction distribution as the real cluster sky positions. We show the distribution of extinction values of our real and random data sets in Figure 8. Notice the deficit of clusters in regions of high column density when compared with positions randomly chosen over the same region of sky as our survey. This was first seen by Peacock & West (1992) and later quantified by Nichol & Connolly (1996).

The redshifts assigned to the random catalog points are selected from the observed data after being smoothed with a Gaussian of width 3000 km s^{-1}. This technique corrects for radial density gradients on small scales in the observed distribution. For the whole-sky sample, the random points with $\delta \geq -27^\circ$ are assigned redshifts from the Abell clusters, while the points with $\delta \leq -27^\circ$ are assigned redshifts from the ACO catalog.

Figure 9 shows the results for the spatial correlation function for samples 1 and 2. The three lines on the graphs indicate two enveloping limits that span the results of Bahcall & Soniera (1983) and Dalton et al. (1994a) ($r_o = 25$, $\gamma = -1.8$ and $r_o = 15$, $\gamma = -2.0$) and the best power-law fit for $\xi(r)$ from our data points (from $r = 4.5$ h^{-1} Mpc to 56 h^{-1} Mpc). The error bars plotted in Figure 9 are determined from

$$\delta\xi = \frac{(1+\xi)}{\sqrt{\mathrm{DD}}} \, . \tag{8}$$

There are multiple methods for determining the errors on ξ, including the bootstrap technique (Barrow, Sonoda, & Bhavsar 1984). The bootstrap technique involves removing one or more clusters from the sample and recalculating ξ. This procedure is implemented many times, and the variance in ξ is then calculated. However, removed data points are often members of true large-scale structures. Thus, by removing clusters, you are actually altering the true structure in the catalog. This could result in a serious overestimation of the errors. On the other hand, Poisson-type errors (e.g., eq. [8]) assume that there is no structure in the catalog and therefore underestimate the true uncertainties in ξ. This has been shown to be the case by Croft & Efstathiou (1994), who find that equation (8) underestimates the true error by a factor of $\simeq$1.5. We have excluded the bins of smaller separations ($r \leq 4.5$ h^{-1} Mpc) from the fit for the following reasons: (1) the number of data-data pairs at small separations becomes

TABLE 5

RESULTS FOR THE POWER-LAW FITS OF ξ

Sample $R \geq 1, \lvert b\rvert > 30^\circ$	Size	γ	r_o (h^{-1} Mpc)
Sample 1	338	-2.03 ± 0.3	$18.6^{-2.7}_{+2.4}$
Sample 2	598	-1.95 ± 0.2	$21.0^{-2.2}_{+2.0}$
Sample 2[a]	592	-2.00 ± 0.2	$20.7^{-2.2}_{+2.1}$
Sample 2[b]	592	-1.90 ± 0.2	$20.1^{-2.3}_{+2.2}$
Sample 2[c]	592	-2.09 ± 0.2	$20.7^{-2.3}_{+2.3}$
Sample 2[d]	580	-1.87 ± 0.2	$19.0^{-2.4}_{+2.3}$
Sample 2[e]	598	-2.04 ± 0.2	$21.1^{-2.2}_{+2.1}$
Sample 2[f]	462	-2.10 ± 0.2	$19.1^{-3.1}_{+2.9}$
Sample 2[g]	634	-2.08 ± 0.2	$19.3^{-2.0}_{+2.0}$

[a] Members of Corona Borealis supercluster removed.
[b] Members of Microscopium supercluster removed.
[c] Members of Aquarius supercluster removed.
[d] Members of all three superclusters removed.
[e] After rotation of superclusters.
[f] All clusters with $\geq$2 measured galaxies.
[g] All $R \geq 1$ ACO clusters included.

unreasonably small; (2) we get nearer to the actual diameter of a rich Abell cluster where projection effects compromise differentiation from a foreground and background cluster; and (3) the $\simeq$500 km s^{-1} cluster peculiar velocities will mask structure. The results for the power-law fits to ξ are listed in Table 5.

6.1. *Effects of Superclusters on* r_o

The effect of the Corona Borealis supercluster (Cor Bor) on the amplitude of the correlation was illustrated in Postman, Geller, & Huchra (1988) and again in PHG92. Using the Bahcall & Soniera (1983) $D \leq 4$, $R \geq 1$ sample of clusters, Postman et. al (1988) concluded that Cor Bor was responsible for $\simeq$30% of the power in $\xi(r)$. They later reexamined this effect using a larger sample of $R \geq 1$ clusters and found that Cor Bor contributed slightly less, $\simeq$20% (PHG92). Using sample 2, we find little or no change in r_o after removing Cor Bor (see Table 5). Such a result should be expected if the effect of dense and compact superclusters on r_o decreases as the sample size increases. However, Cor Bor is not the only dense and compact supercluster. Batuski et al. (1999) examined the Abell/ACO catalog for superclustering and find two new dense and compact superclusters in Microscopium and Aquarius. The Microscopium supercluster consists of A3677, A3682, A3691, A3693, A3695, and A3705 and was first reported by Zucca et al. (1993) and many redshifts were observed by ENACS (Katgert et al. 1996). The Aquarius supercluster "knot" was discovered by Batuski et al. (1999) and consists of A2546, A2553, A2554, A2555, A2579, and A3996. After excluding all three of these dense and compact superclusters, we find little change in the slope or correlation length (see Table 5). This suggests that our sample is large enough not to be affected by large and localized fluctuations in the density field of the nearby universe. In other words, the $R \geq 1$ Abell/ACO clusters represent a fair sample of the universe to $z \sim 0.14$. (We note that most of the Shapley Concentration does not appear in these analyses because of the imposed galactic latitude limit of $|b| \geq 30^\circ$.)

6.2. *Anisotropy in the Abell Catalog*

As discussed in § 1, there have been claims that the Abell catalogs contain spurious clusters caused by projection. The tool to identify spurious clustering involves separating the two-point spatial correlation function into two components: one along the line of sight and the other perpendicular to the line of sight, with r_1 and r_2 being the line-of-sight distance between two clusters (Sutherland 1988):

$$R^2 = \sigma^2 + \pi^2 \, , \tag{9}$$

where

$$\pi = |r_1 - r_2| \, . \tag{10}$$

One then looks for elongations (anisotropies) in the contours of $\xi(\sigma,\pi)$ along the line of sight.

Figure 10 shows contour plots of $\xi(\sigma,\pi)$ over the range 0–100 h^{-1} Mpc for both σ and π, in 10 h^{-1} Mpc bins. The heavy contour line is $\xi(\sigma,\pi) = 1$, indicating relatively strong correlations. The contour plot of sample 1 looks similar to that presented in Miller et al. (1999a). The small amount of anisotropy in the range $\sigma < 10\ h^{-1}$ Mpc and $20 \leq \pi \leq 40$ h^{-1} Mpc is the result of the Corona Borealis and Ursa Majoris superclusters (both filamentary and within 25° of the line of sight).

Our larger cluster sample contains the Aquarius supercluster (Batuski et al. 1999). This supercluster is highly

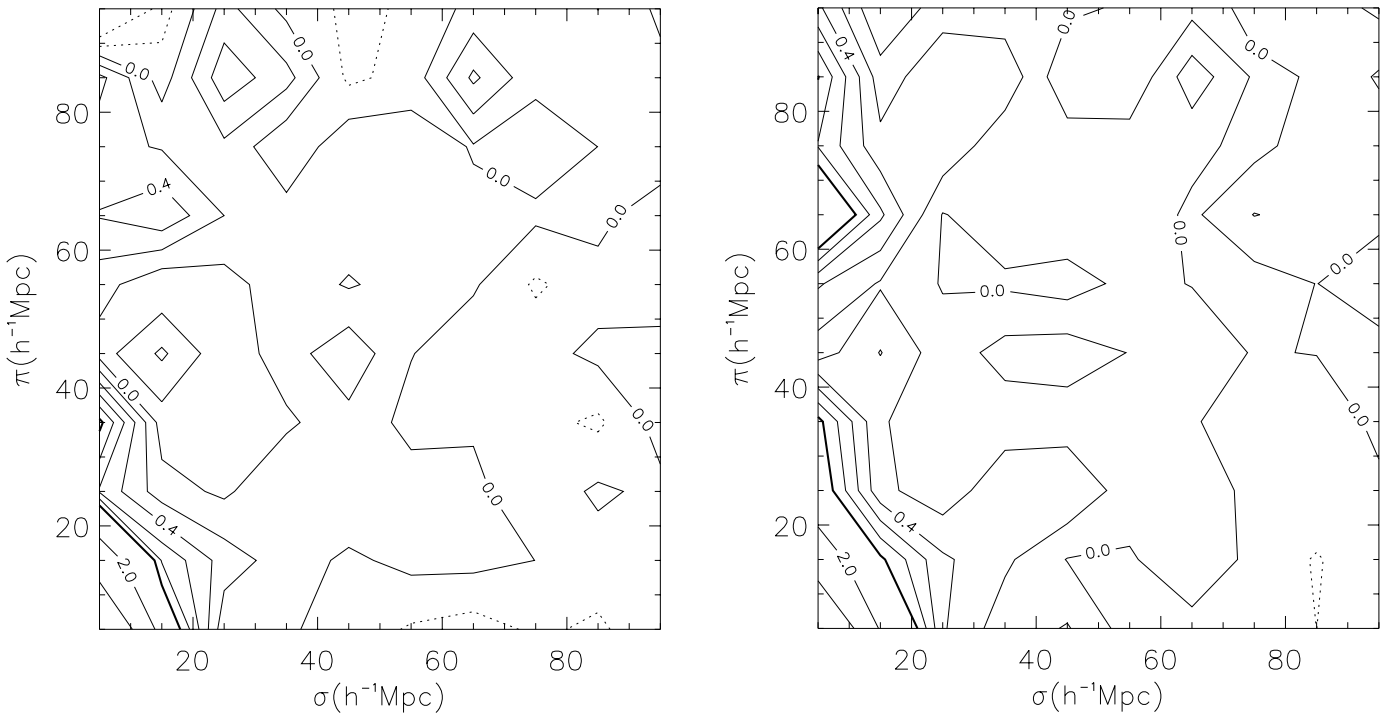

FIG. 10.—Spatial correlation function contours. *Left*: Contour plot of $\xi(\sigma,\pi)$ for sample 1. *Right*: Contour plot of $\xi(\sigma,\pi)$ for sample 2. Notice the small amount of anisotropy near $\sigma = 10\,h^{-1}$ Mpc and $\pi = 60\,h^{-1}$ Mpc.

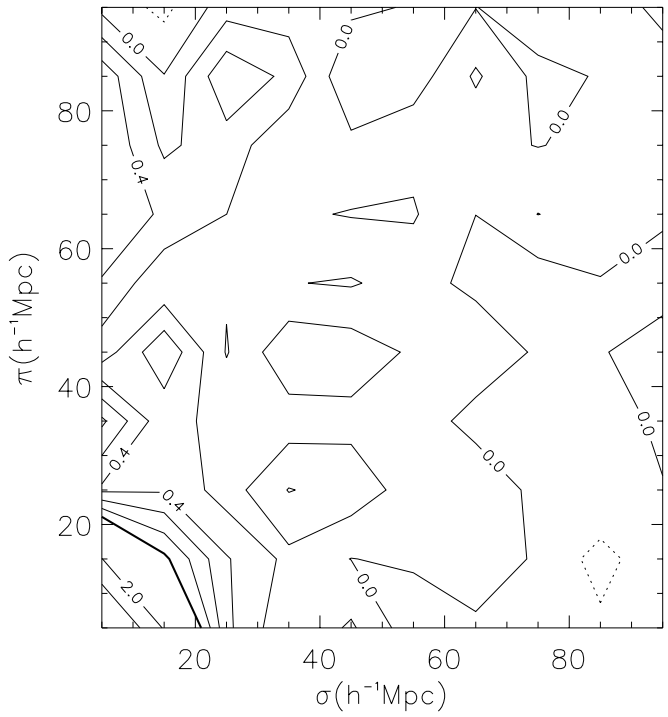

FIG. 11.—Plot of $\xi(\sigma,\pi)$ in 10 h^{-1} Mpc bins for the whole-sky magnitude-limited sample after rotating the Ursa Majoris, Corona Borealis, and Aquarius superclusters. Compare with Fig. 10.

extended ($\simeq$100 h^{-1} Mpc) and oriented within about 6° of the line of sight. One might predict that such a large number of clusters nearly along the line of sight would create anisotropies in $\xi(\sigma,\pi)$ at scales near the length of the supercluster, since the Aquarius filament contains many cluster pairs with 50–75 h^{-1} Mpc radial separations. In fact, we see in the right side of Figure 10 that $\xi(\sigma,\pi) \sim 1$ for $\pi \simeq 60$ h^{-1} Mpc and $\sigma \simeq 10\,h^{-1}$ Mpc.

To test whether superclusters are the root cause of these anisotropies, we determined which cluster pairs were causing the excess in $\xi(\sigma,\pi)$ for $\pi \geq 30$ h^{-1} Mpc in sample 2. We found that most of the cluster pairs are members of Corona Borealis, Ursa Majoris, and the Aquarius superclusters. As in Miller et al. (1999a), we rotate these superclusters until their semimajor axes are perpendicular to the line of sight. We then recalculated the standard two-point correlation function and found no difference in the amplitude or slope (see Table 5). Figure 11 shows the isocontours of $\xi(\sigma,\pi)$ for the new whole-sky volume-limited sample (sample 2) with the rotated superclusters. The reader might note that this rotation does not cause the contours of ξ to become flattened perpendicular to the line of sight. This is because our cluster sample is large enough so that this rotation only increases the number of pairs perpendicular to the line of sight by less than 5%, far too small to cause any noticeable changes perpendicular to the line of sight. On the other hand, the catalog has very few pairs along the line of sight, thus we see a significant difference in $\xi(\pi)$ after the rotation.

Notice that the anisotropies are no longer present (compared with Fig. 10). We can draw two conclusions from this exercise: (1) the anisotropies in $\xi(\sigma,\pi)$ can be attributed to real clustering along the line of sight and (2) the presence of these anisotropies does not affect the amplitude or slope of the correlation function.

To summarize our correlation function analyses, we find that the slopes and correlation lengths for subsets of sample 2 fall within 1 σ of each other: $18.6 \leq r_o \leq 21.1\ h^{-1}$ Mpc and $-2.10 \leq \gamma \leq -1.86$. We also checked the effect of excluding the poorest ACO clusters by putting back in the ACO clusters that have $R \geq 1$ and $N_{\mathrm{gal}} < 60$ and recalculating the two-point function. We find no significant difference in the slope or amplitude compared with sample 2. We also measured the two point spatial correlation function for only those clusters having two or more measured galaxy redshifts, and again we find no significant difference in our conclusions. The increased number of redshifts, in addition to the increased accuracy of those redshifts because of multiple galaxy observations, have produced a much improved fit (with much smaller errors) to the rich cluster correlation function. Table 5 also shows that the correlation function for Abell/ACO $R \geq 1$ clusters is very robust.

7. SUMMARY

The MX Northern Abell Cluster Survey has met with a great deal of observational success, as well as luck. During the 8 yr period over which the observations occurred, we were able to collect data on every run. The results of the total survey (i.e., parts I and II combined) can be summarized as follows:

1. We have measured 195 new mean cluster redshifts for those clusters in the region $0^{\mathrm{h}} \leq \alpha \leq 24^{\mathrm{h}}$ and $-17° \leq \delta \leq 90°$, excluding $|b| < 30°$.
2. We have also found that seven Abell clusters are chance projections of galaxies along the line of sight.
3. We have observed an average of eight galaxy redshifts per cluster field that turned out to be members.

This survey has increased the number of clusters with measured redshifts having $m_{10} \leq 17.0$ and $-27° \leq \delta \leq 90°$ to a total sample of 350 out of 368 possible clusters. We have also used our data, along with redshifts from the literature, to create the largest volume-limited samples of clusters yet assembled. The 598 clusters in our largest sample is nearly 5 times the number of the earliest $R \geq 1$ cluster samples used for large-scale structure analyses. This deeper (in magnitude) and more complete sample of rich Abell clusters provides an excellent database on which statistical analyses of large-scale structure can be performed.

We have calculated the two-point correlation function with greatly reduced uncertainty and much smaller errors, especially on larger scales. Miller & Batuski (2001) have recently performed a power spectrum analysis on samples 1 and 2 described in § 5. They show that these cluster samples are large enough to trace structure to scales over 300 h^{-1} Mpc. In fact, the samples presented in § 5 are the only cluster sets with large enough volumes to differentiate between various standard cosmological models (Miller & Batuski 2001). Other analyses, such as the cluster luminosity function, the distribution of velocity dispersions, and the mass functions, can also be conducted on this catalog with much less uncertainty of cluster properties.

We have used the largest rich cluster data set available to calculate the two-point spatial correlation function, ξ, and also look for line-of-sight anisotropies within the Abell/

ACO catalogs. Our results for the power-law fits to $\xi(r)$ are presented in Figure 9 and Table 5. We find that the existence of highly dense and compact superclusters, such as the Corona Borealis supercluster (Cor Bor), do not strongly affect the amplitude of the two-point function. The amplitude and slope of the two-point spatial correlation function of Abell/ACO clusters are very robust. The REFLEX X-ray–selected cluster catalog is the next largest (in number) cluster sample used in two-point function analyses (Collins et al. 2000). Using 449 clusters, they find $r_o = 18.8 \pm 0.8\ h^{-1}$ Mpc and $\gamma = -1.83^{+0.15}_{-0.08}$ compared with our results, which find $18.6 \leq r_o \leq 21.0\ h^{-1}$ Mpc and $-2.03 \leq \gamma \leq -1.95$ for samples 1 and 2. It is satisfying to note that these two independently selected tracers of large-scale structure find nearly identical results for the distribution of luminous matter on large scales.

The authors would like to thank Dennis Means and Vic Hansen for assistance during observing runs, as well as Elizabeth Rizza for her work installing new fibers in MX in 1997. We also thank the referee for helpful comments and suggestions. In addition we thank the Steward Observatory telescope allocation committee for providing observing time on the Bok 2.3 m telescope. Funding was provided to C. J. M., K. S. K., and D. J. B. by NASA/EPSCoR through the Maine Space Grant Consortium and to J. M. H. by the Large Binocular Telescope Project.

REFERENCES

Abadi, M., Lambas, D., & Muriel, H. 1998, ApJ, 507, 526
Abell, G. O. 1958, ApJS, 3, 211
Abell, G. O., Corwin, H. G., & Olowin, R. P. 1989, ApJS, 70, 1
Bahcall, N. A., & Cen, R. 1994, ApJ, 426, L15
Bahcall, N. A., & Soniera, R. 1983, ApJ, 270, 20
Bahcall, N. A., & West, M. J. 1992, ApJ, 392, 419
Barrow, J. D., Sonoda, D. H., & Bhavsar, S. P. 1984, MNRAS, 210, 19P
Batuski, D., Bahcall, N., Burns, J., & Olowin, R. 1989, ApJ, 341, 599
Batuski, D., Miller, C., Slinglend, K., Balkowski, C., Maurogordato, S., Cayette, V., Felenbok, P., & Olowin, R. 1999, ApJ, 520, 491
Bautz, L., & Morgan, W. 1970, ApJ, 162, L149
Beers, T. C., Flynn, K., & Gebhardt, K. 1990, AJ, 100, 32
Borgani, S., Plionis, M., & Kolokotronis, V. 1999, MNRAS, 305, 866
Broadhurst, T., Ellis, R., Koo, D., & Szalay, A. 1990, Nature, 343, 726
Burke, D. J., Collins, C. A., & Mann, R. G. 2000, ApJ, 532, L105
Colless, M., et al. 2001, MNRAS, 328, 1039
Collins, C. A., et al. 2000, MNRAS, 319, 939
Croft, R. A. C., Dalton, G. B., Efstathiou, G., Sutherland, W. J., & Maddox, S. J. 1997, MNRAS, 291, 305
Croft, R. A. C., & Efstathiou, G. 1994, MNRAS, 267, 390
Cruddace, R., et al. 2002, ApJS, 140, 239
Dalton, G. B., Croft, R., Efstathiou, G., Sutherland, W., Maddox, S., & Davis, M. 1994a, MNRAS, 271, L47
Dalton, G. B., Efstathiou, G., Maddox, S. J., & Sutherland, W. J. 1992, ApJ, 390, L1
———. 1994b, MNRAS, 269, 151
Donahue, M., et al. 2001, ApJ, 552, L93
———. 2002, ApJ, 569, 689
Ebeling, H., Edge, A., Fabian, A., Allen, S., Crawford, C., & Bohringer, H. 1997, ApJ, 479, L101
Ebeling, H., Voges, W., Bohringer, H., Edge, A. C., Huchra, J. P., & Briel, U. G. 1996, MNRAS, 281, 799
Efstathiou, G., Dalton, G., Maddox, S., & Sutherland, W. 1992, MNRAS, 257, 125
Eke, V. R., Cole, S., Frenk, C. S., & Navarro, J. F. 1996, MNRAS, 281, 703
Geller, M., & Huchra, J. 1989, Science, 246, 897
Hamilton, A. 1993, ApJ, 417, 19
Hill, J., & Lesser, M. 1986, Proc. SPIE, 627, 303
Jing, Y., Plionis, M., & Valdarnini, R. 1992, ApJ, 389, 499
Jones, C., & Forman, W. 1999, ApJ, 511, 65
Katgert, P., et al. 1996, A&A, 310, 8
Kolb, E. W., & Turner, M. S. 1990, The Early Universe (Reading: Addison-Wesley)
Leir, A. A., & van den Bergh, S. 1977, ApJS, 34, 381
Lewis, I. J., Glazebrook, K., & Taylor, K. 1998, Proc. SPIE, 3355, 828
Maddox, S. J., Efstathiou, G., & Sutherland, W. J. 1990a, MNRAS, 246, 433
Maddox, S. J., Efstathiou, G., Sutherland, W. J., & Loveday, J. 1990b, MNRAS, 243, 692
Miller, C. J., & Batuski, D. J. 2001, ApJ, 551, 635
Miller, C. J., Batuski, D. J., Slinglend, K., & Hill, J. 1999a, ApJ, 523, 492
Miller, C. J., Ledlow, M., & Batuski, D. 1999b, MNRAS, submitted (astro-ph/9906423)
Moscardini, L., Matarrese, S., De Grandi, S., & Lucchin, F. 2000, MNRAS, 314, 647
Narlikar, J. V. 1983, Introduction to Cosmology (Cambridge: Cambridge Univ. Press)
Nichol, R., Briel, U., & Henry, J. 1994, MNRAS, 267, 771
Nichol, R., Collins, C., Guzzo, L., & Lumsden, S. 1992, MNRAS, 255, 21P
Nichol, R., & Connolly, A. 1996, MNRAS, 279, 521
Oke, J. B., & Sandage, A. 1968, ApJ, 154, 21
Peacock, J., & West, M. 1992, MNRAS, 259, 494
Pinkney, J., Rhee, G., Burns, J., Hill, J., Oegerle, W., Batuski, D., & Hintzen, P. 1993, ApJ, 416, 36
Postman, M., Geller, M., & Huchra, J. P. 1988, AJ, 95, 267
Postman, M., Huchra, J. P., & Geller, M. 1986, AJ, 92, 1238
———. 1992, ApJ, 384, 404 (PHG92)
Postman, M., Huchra, J. P., Geller, M. J., & Henry, J. P. 1985, AJ, 90, 1400
Press, W. H., Rybicki, G. B., & Hewitt, J. N. 1992, ApJ, 385, 404
Quintana, H., Melnick, J., Proust, D., & Infante, L. 1997, A&AS, 125, 247
Quintana, H., & Ramirez, A. 1995, ApJS, 96, 343
Ratcliffe, A., Shanks, T., Parker, Q., & Fong, R. 1998, MNRAS, 296, 173
Retzlaff, J., Borgani, S., Gottlöber, S., Klypin, A., & Müller, V. 1998, NewA, 3, 631
Romer, A. K., Collins, C. A., Bohringer, H., Cruddace, R. G., Ebeling, H., MacGillivray, H. T., & Voges, W. 1994, Nature, 372, 75
Romer, K., et al. 2000, ApJS, 126, 209
Rowan-Robinson, M., et al. 1990, MNRAS, 247, 1
Saunders, W., et al. 2000, in ASP Conf. Ser. 201, Cosmic Flows Workshop, ed. S. Courteau & J. Willick (San Francisco: ASP), 223
Schlegel, D., Finkbeiner, D., & Davis, M. 1998, ApJ, 500, 525
Scott, E. L. 1957, AJ, 62, 248
Shectman, S., Landy, S., Oemler, A., Tucker, D. L., Lin, H., Kirshner, R., & Schecter, P. 1996, ApJ, 470, 172
Slinglend, K., Batuski, D., Miller, C., Haase, S., Michaud, K., & Hill, J. 1998, ApJS, 115, 1
Smoot, G., et al. 1992, ApJ, 396, L1
Struble, M., & Rood, H. 1991, ApJS, 77, 363
———. 1999, ApJS, 125, 35
Sutherland, W. 1988, MNRAS, 234, 159
Tonry, J., & Davis, M. 1979, AJ, 84, 1511
West, M., & van der Bergh, S. 1991, ApJ, 373, 1
Willmer, C., Da Costa, L. N., & Pellegrini, P. S. 1998, AJ, 115, 869
York, D. G., et al. 2000, AJ, 120, 1579
Zabludoff, A., Geller, M., Huchra, J., & Vogeley, M. 1993, AJ, 106, 1273
Zucca, E., Zamorani, G., Scaramella, R., & Vettolani, G. 1993, ApJ, 407, 470